



# TESS Giants Transiting Giants. IV. A Low-density Hot Neptune Orbiting a Red Giant Star

Samuel K. Grunblatt<sup>1</sup> , Nicholas Saunders<sup>2,15</sup> , Daniel Huber<sup>2</sup> , Daniel Thorngren<sup>1</sup> , Shreyas Vissapragada<sup>3,16</sup> ,  
Stephanie Yoshida<sup>3</sup> , Kevin C. Schlaufman<sup>1</sup> , Steven Giacalone<sup>4,15</sup> , Mason Macdougall<sup>5</sup> , Ashley Chontos<sup>2,6,15</sup> ,  
Emma Turtelboom<sup>4</sup> , Corey Beard<sup>7</sup> , Joseph M. Akana Murphy<sup>8,15</sup> , Malena Rice<sup>9</sup> , Howard Isaacson<sup>4,10</sup> ,  
Ruth Angus<sup>11,12,13</sup> , and Andrew W. Howard<sup>14</sup>

<sup>1</sup> William H. Miller III Department of Physics and Astronomy, Johns Hopkins University, 3400 N Charles Street, Baltimore, MD 21218, USA

<sup>2</sup> Institute for Astronomy, University of Hawai'i at Mānoa, 2680 Woodlawn Drive, Honolulu, HI 96822, USA

<sup>3</sup> Department of Astronomy, Harvard University, 60 Garden Street, Cambridge, MA 02138, USA

<sup>4</sup> Department of Astronomy, University of California Berkeley, Berkeley, CA 94720, USA

<sup>5</sup> Department of Physics & Astronomy, University of California Los Angeles, Los Angeles, CA 90095, USA

<sup>6</sup> Department of Astrophysical Sciences, Princeton University, 4 Ivy Lane, Princeton, NJ 08544, USA

<sup>7</sup> Department of Physics & Astronomy, University of California Irvine, Irvine, CA 92697, USA

<sup>8</sup> Department of Astronomy and Astrophysics, University of California, Santa Cruz, CA 95064, USA

<sup>9</sup> Department of Astronomy, Yale University, New Haven, CT 06511, USA

<sup>10</sup> Centre for Astrophysics, University of Southern Queensland, Toowoomba, QLD 4350, Australia

<sup>11</sup> American Museum of Natural History, 200 Central Park West, Manhattan, NY 10024, USA

<sup>12</sup> Center for Computational Astrophysics, Flatiron Institute, 162 5th Avenue, Manhattan, NY 10010, USA

<sup>13</sup> Department of Astronomy, Columbia University, 550 West 120th Street, New York, NY 10027, USA

<sup>14</sup> Cahill Center for Astronomy & Astrophysics, California Institute of Technology, Pasadena, CA 91125, USA

Received 2024 February 14; revised 2024 April 5; accepted 2024 April 11; published 2024 June 5

## Abstract

Hot Neptunes, gaseous planets smaller than Saturn ( $\sim 3\text{--}8 R_{\oplus}$ ) with orbital periods less than 10 days, are rare. Models predict this is due to high-energy stellar irradiation stripping planetary atmospheres over time, often leaving behind only rocky planetary cores. Using our TESS full-frame-image pipeline `giants` in conjunction with Keck/HIRES radial velocity measurements, we present the discovery of TIC365102760 b, a  $6.2 R_{\oplus}$  ( $0.55 R_J$ ),  $19.2 M_{\oplus}$  ( $0.060 M_J$ ) planet transiting a red giant star every 4.21285 days. The old age and high equilibrium temperature yet remarkably low density of this planet ( $\rho_p = 0.58_{-0.20}^{+0.30} \rho_J$ ) suggest that its gaseous envelope should have been stripped by high-energy stellar irradiation billions of years ago. The present-day planet mass and radius suggest the atmospheric stripping was slower than predicted. Unexpectedly low stellar activity and/or late-stage planet inflation could be responsible for the observed properties of this system. Further studies of this system with more precise photometry in multiple passbands will be capable of revealing more details of this planet's atmosphere.

*Unified Astronomy Thesaurus concepts:* [Exoplanet detection methods \(489\)](#); [Star-planet interactions \(2177\)](#); [Red giant branch \(1368\)](#); [Exoplanet atmospheric evolution \(2308\)](#); [Hot Neptunes \(754\)](#)

## 1. Introduction

Over the last 30 yr, the discovery of over 5000 exoplanets has revealed that planetary system architectures are incredibly diverse (Berger et al. 2020; Rosenthal et al. 2021). One of the most striking demographic features of this sample is the dearth of planets with masses and radii similar to Neptune on short periods (Mazeh et al. 2016). Star–planet interactions, including atmospheric effects like inflation (Guillot et al. 1996) and photoevaporation (Vidal-Madjar et al. 2004) and secular processes like high-eccentricity migration (Matsakos & Königl 2016; Owen & Lai 2018), have been shown to be responsible for this feature of planet demographics.

One of the most poorly constrained processes governing planetary system architectures is the tidal interaction between

the planet and the star (Ogilvie 2014). Tides on the star and planet can lead to planet heating, inspiral, and tidal locking, processes whose efficiencies are not well tested due to the extreme conditions required to test them (Barker 2020; Dewberry & Wu 2024). Short-period planets around giant stars are expected to experience the most extreme tidal forces of all planetary systems. However, the characterization of the planet population on short-period orbits around giants suggests that this population is similar to the planet population orbiting main-sequence stars, which is unexpected, given the much stronger tidal forces at play in evolved systems (Grunblatt et al. 2019). The detection of a wide range of planets on short-period orbits around giant stars is essential for testing tidal theory and constraining the efficiencies of tidal planet inflation and inspiral (Villaver et al. 2014; Hamer & Schlaufman 2019; Grunblatt et al. 2022). Fewer than 20 such planets have been found to date.

The Transiting Exoplanet Survey Satellite (TESS) has successfully confirmed more than 200 planets with orbital periods of less than 10 days since 2018 (Guerrero et al. 2021). Several of these planets have shown clear evidence for radius inflation (Rodríguez et al. 2021; Grunblatt et al. 2022;

<sup>15</sup> NSF Graduate Research Fellow.

<sup>16</sup> 51 Pegasi b Fellow.



Yee et al. 2022). Others are expected to have undergone significant atmospheric mass loss in their lifetimes (Jenkins et al. 2020; Persson et al. 2022). Approximately 5% of these systems orbit giant stars (Saunders et al. 2022; Grunblatt et al. 2023). As inflated planets are more susceptible to mass loss, a process that continues over the lifetime of the planet, the characterization of inflated planets around post-main-sequence, evolved ( $T_{\text{eff}} < 6000 \text{ K}$ ,  $R > 2 R_{\odot}$ ) stars nearing the ends of their lives can constrain the timescales for planetary mass-loss and inflation mechanisms. Evidence for the extended atmospheres of inflated planets transiting evolved stars, a possible indicator of atmospheric mass loss, has already been identified (Mounzer et al. 2022).

Here we introduce the fourth discovery in an installment of discoveries from the TESS Giants Transiting Giants (GTG) program (Grunblatt et al. 2022, 2023; Saunders et al. 2022; Pereira et al. 2024). This program is specifically targeted to detect planets transiting red giant stars, which are often missed by other searches for transiting planets, due to the long transit duration and unique stellar noise properties of evolved stars. This planet is unique among the TESS GTG sample, in that unlike the previous hot-Jupiter-like planets found by this survey, this planet is close in mass to Neptune, but more closely resembles Saturn in size and density. In addition, this planet is one of the most irradiated Neptune-mass planets and the most irradiated Neptune-mass planet orbiting a post-main-sequence star currently known. Characterizing this planet will help constrain the late-stage evolution of planetary atmospheres.

## 2. Observations

### 2.1. TESS Photometry

TIC 365102760 b was discovered as part of the TESS GTG survey identifying new planets around evolved host stars. Using version 8 of the TESS input catalog (TIC; Stassun et al. 2019), we followed the cuts of Grunblatt et al. (2019) based on color, magnitude, and Gaia parallax in order to limit our sample to evolved stars. We developed the `giants`<sup>17</sup> Python package for accessing, detrending, and searching TESS observations for periodic transit signals. The details of how this pipeline processes TESS full-frame-image (FFI) data are described in Saunders et al. (2022).

TIC 365102760 was observed in TESS sectors 14, 15, 16, 41, 55, and 56 between 2019 July 18 and 2019 October 7, 2021 July 23 and 2021 August 20, and 2022 August 5 and 2022 September 30. Optical photometry was first acquired at a 30 minute cadence in 2019, at a 10 minute cadence in 2021, and at 200 s and 2 minute cadences in 2022. We produced a light curve with both a 30 minutes and a 10 minutes cadence using the `giants` package. We also produced a light curve for this target using the `eleanor` package (Feinstein et al. 2019). In addition, light curves for this target were produced by the TESS science team Quick Look Pipeline (QLP) using both simple aperture photometry (SAP) as well as a Kepler-like signal processing algorithm (KSPSAP). Subsequently, the SPOC pipeline (Jenkins et al. 2010, 2016), which has been tested on a significantly larger number of planetary transit data sets than the other pipelines mentioned here, produced a light curve for the 120 s, high-cadence data, which we also use in

our analysis. We present these five light curves for TIC 365102760 in Figure 1.

In addition to TIC 365102760, we used our `giants` pipeline to produce TESS light curves for as many red giant branch stars with TESS magnitude  $m_T < 13$  as possible. We produced light curves for approximately 540,000 stars from the first 2 yr of data from the TESS mission. We performed an automated box least-squares (BLS; Kovács et al. 2002) search on all targets and produced summary plots displaying the BLS output as well as TIC information and the TESS FFI pixel cutout. These summary plots were then visually inspected, during which this candidate was flagged for potential rapid ground-based follow-up. We illustrate the BLS results for all light curves of TIC 365102760 considered in this work in Figure 2 and corresponding phase-folded light curves of TIC 365102760 in Figure 3.

The 4.2 day transit signal from the planet is detected clearly above the noise floor in the BLS searches of the `giants` and the 2 minute cadence SPOC light curves ( $\geq 4\sigma$ ), but is not recovered in the other light curves. This is likely related to the principal component detrending as well as the median smoothing filter of the `giants` light curve, which is broader than that of the KSPSAP light curve but still results in a much smoother light curve than pure SAP (as can be seen in Figure 1). We note that in Figure 3, the transit can just barely be perceived by eye at a phase of 0.0 day in the `giants` and SPOC light curves, but is not visually detectable in the other light curves presented here.

Given the relatively weak planet transit signal, this planet did not reach the TESS team criteria to be flagged as a TESS object of interest, and thus was not prioritized for ground-based follow-up by the larger TESS follow-up program. This planet would not have been discovered if not for the GTG survey. Thus, it was important for our team to independently verify the existence of a planetary signal around this star.

### 2.2. Radial Velocity Measurements

Radial velocity (RV) observations were taken with the HIRES spectrograph on the Keck I telescope on Maunakea, Hawaii (Vogt et al. 1994). HIRES has a resolving power of  $R \approx 60,000$  and wavelength coverage between  $\sim 350$  and  $\sim 800 \text{ nm}$ . 20 RV measurements were taken of TIC 365102760 between 2021 June 13 and 2022 July 11. We list our RV measurements of TIC 365102760 in Table 1.

Using these RV measurements alone, we also search for an independent signal in the data. Using the software package `RVsearch` (Rosenthal et al. 2021), we convert the RV measurements to a periodogram, which accounts for the systematic signals of the Earth and Moon orbital and rotational periods. We find that a signal at 4.20 days is recovered with high significance, matching the planet transit period seen in the `giants` light curve. This signal falls just short of the false-alarm probability cutoff used for RV-only planet confirmation. We illustrate the detection of this signal in our RV data in Figure 4. This independent confirmation of a planetary signal, observed with the same period and phase as seen in the `giants` light curve, makes the planet scenario significantly more likely than either data set would on its own and thus allows us to confirm this planet as real. We describe our model of the planet transit in Section 4.

<sup>17</sup> <https://github.com/nksaunders/giants>

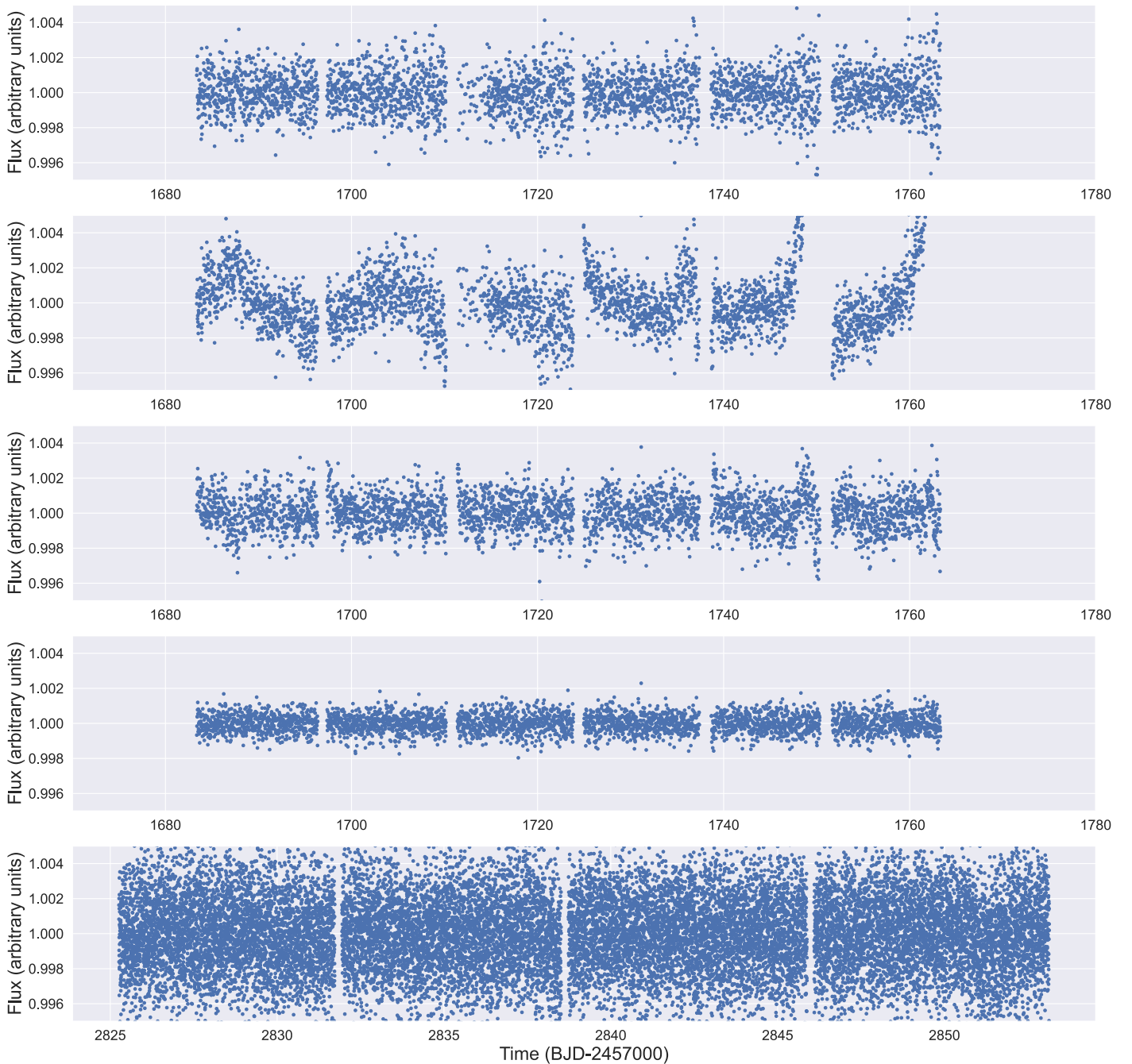


**Figure 1.** Full TESS prime mission light curves of TIC 365102760, produced using the Quick Look Pipeline (QLP) KSPSAP detrending, the QLP SAP detrending, the `eleanor` pipeline, and the `giants` pipeline, from top to second from bottom. Additional data have since been acquired by the TESS extended mission at higher cadence for TIC 365102760 and converted into a light curve via the SPOC pipeline, plotted in the bottom row. The scatter is noticeably higher for the high-cadence light curve.

### 2.3. Visual Companions to TIC 365102760

While TIC 365102760 does not have high-resolution imaging results, the Gaia astrometric noise metric RUWE is low (0.822), and the system is not included in the Gaia eDR3 catalog of binary systems (El-Badry et al. 2021). This indicates that the star is not in a binary system that could be resolved by Gaia photometry and implies no significant dilution in the TESS FFI-generated light curves. This is supported by the consistent transit depth seen in both the SPOC and `giants` light curves, where a dilution correction factor has been applied

to the SPOC light curves only. Since this target was never designated as a TESS object of interest, high-contrast imaging of this target could not be obtained as part of the TESS follow-up observation program. However, no evidence of a spectroscopic binary can be seen in the spectra of this star, placing limits on the significant additional flux in the aperture from a star with a significantly different RV. In addition, the RV measurements of this system do not show evidence for a significant linear or quadratic trend resulting in deviations larger than  $1 \text{ m s}^{-1}$ , ruling out any stellar mass companions within 30 au of the host star. Taken together, the available data

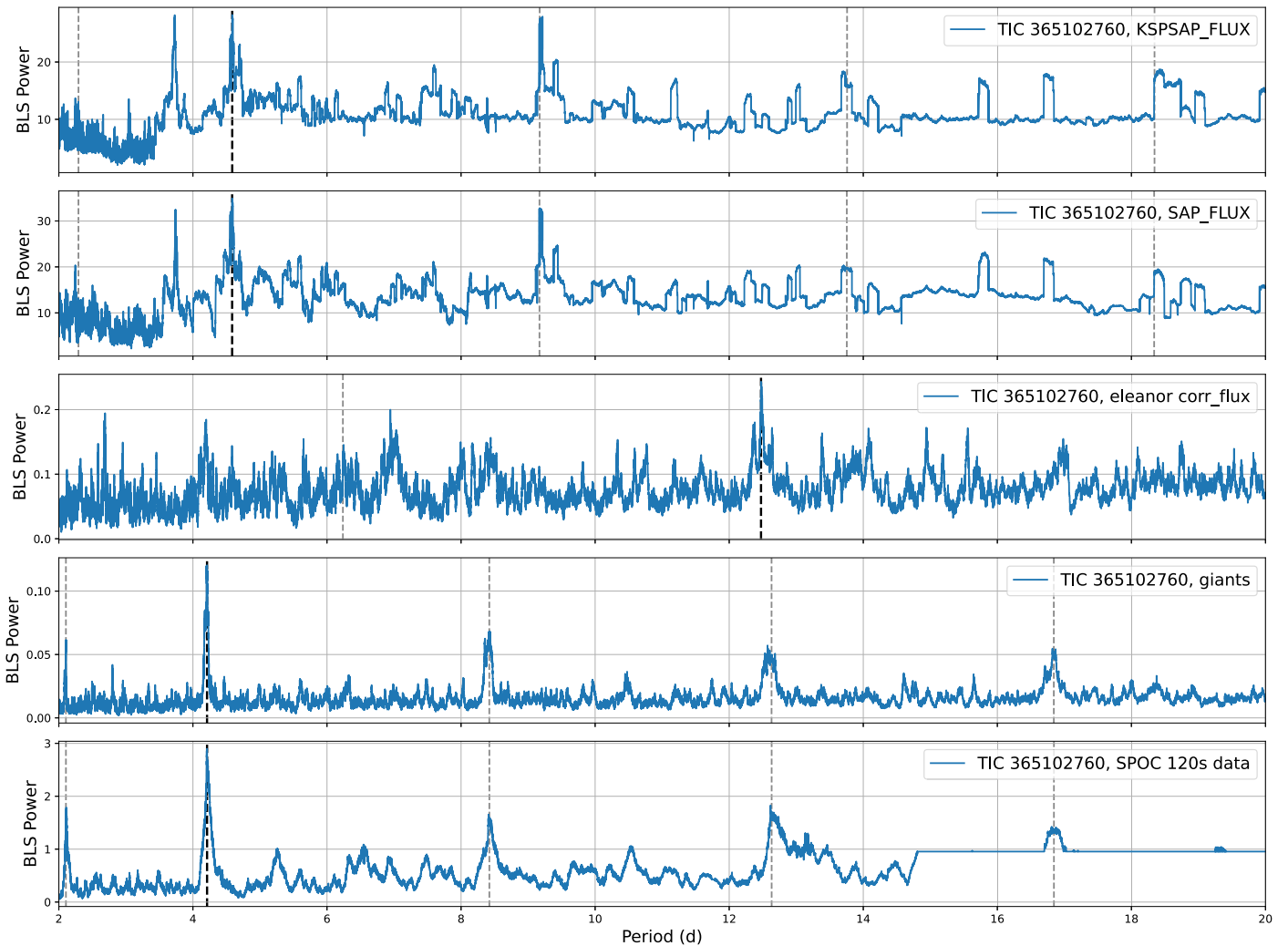


**Figure 2.** BLS power as a function of period for the five light curves of TIC 365102760 shown in Figure 1. The period of highest power has been highlighted with a black dashed line and its harmonics with gray dashed lines. The 4.2 days transit signal is only visible in the *giants* and SPOC light curves, while going undetected in the others.

suggest TIC 365102760 is a single star and not part of a binary system.

### 3. Host Star Characterization

#### 3.1. Spectroscopic and Photometric Analyses

We used *SpecMatch* to measure the metallicity, surface gravity, and effective temperature of the host star from our HIRES template spectrum (Petigura 2015). We then used *isoclassify* (Huber et al. 2017) to combine TICv8 and spectroscopic information to determine the stellar properties for the GTG sample. Figure 5 shows an H-R diagram with evolutionary tracks downloaded from the MESA Isochrones & Stellar Tracks (MIST; Paxton et al. 2011; Choi et al. 2016; Dotter 2016). All GTG systems were fit using *isoclassify* to highlight the relative similarities between them. As all host stars have roughly the same mass and metallicity ( $M_* \approx 1.4 M_\odot$ ,  $[\text{Fe}/\text{H}] \approx 0.25$  dex), we highlight this evolutionary track in red. These systems may extend earlier analyses of “retired A stars” to reveal evolutionary sequences for planetary systems orbiting post-main-sequence, intermediate-mass stars (Johnson et al. 2007, 2010). We find that TIC 365102760 is near the base of the red giant branch stage of evolution.

In addition to the *isoclassify* determination of stellar parameters using *SpecMatch*, we also derive the fundamental and photospheric stellar parameters of TIC 365102760 using the *isochrones* (Morton 2015) package to execute with *MultiNest* (Feroz & Hobson 2008; Feroz et al. 2009, 2019) a simultaneous Bayesian fit of the MIST isochrone grid (Paxton et al. 2011, 2013, 2018, 2019; Choi et al. 2016; Dotter 2016; Jermyn et al. 2023) to a curated collection of data for the star. We fit (1) Gaia DR2 *G* (Gaia Collaboration et al. 2016, 2018; Arenou et al. 2018; Evans et al. 2018; Riello et al. 2018), Two Micron All Sky Survey (2MASS) *JHK<sub>s</sub>* (Skrutskie et al. 2006), and Wide-field Infrared Survey Explorer AllWISE W1W2W3 photometry (Wright et al. 2010; Mainzer et al. 2011); (2) a zero-point-corrected Gaia DR3 parallax (Fabricius et al. 2021; Gaia Collaboration et al. 2021; Lindegren et al. 2021a, 2021b; Rowell et al. 2021; Torra et al. 2021); and (3) an estimated reddening value based on a three-dimensional reddening map (Green et al. 2014, 2019). We use a log uniform age prior between 1 and 10 Gyr, a uniform reddening prior between the estimated reddening value minus/plus five times its uncertainty, and a distance prior proportional to volume between the Bailer-Jones et al. (2021) geometric distance minus/plus five

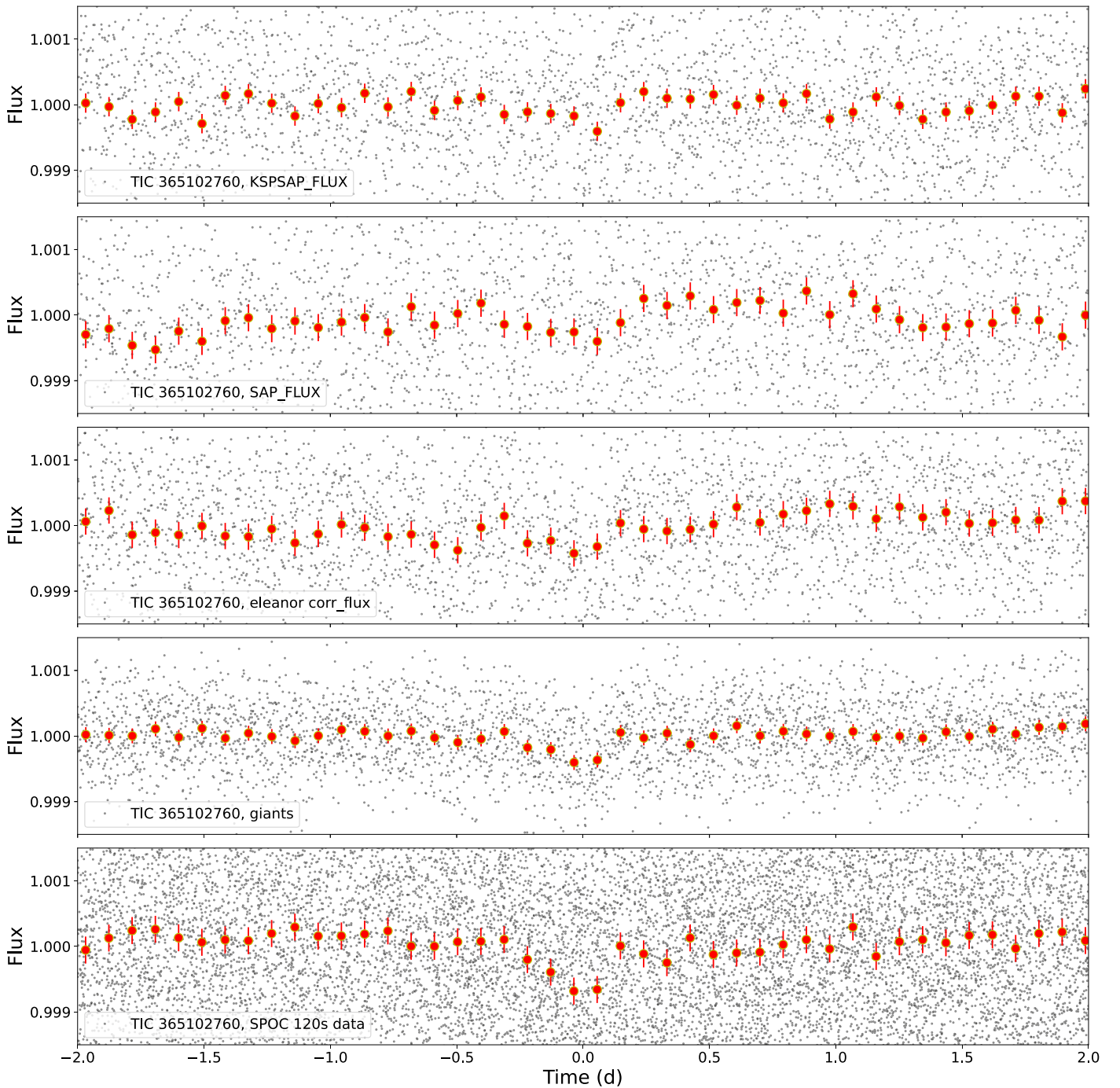


**Figure 3.** Phase-folded light curves showing phase vs. normalized flux of TIC 365102760 using the QLP “KSPSAP FLUX,” “SAP FLUX,” *eleanor*, *giants*, and SPOC pipelines (from top to bottom, respectively). Clear differences in transit depth and shape and light-curve scatter can be seen between the different light curves. The SPOC data cover a shorter baseline (only 27 days) but have a 15 times higher cadence than the other light curves.

times its uncertainty. We plot the results of these analyses in Figure 6.

We find that our fundamental stellar parameter estimates from both approaches agree within uncertainties, and we find that our statistical uncertainties on stellar parameters are smaller for our photometric analysis. Thus, we report the photometrically determined parameters in Table 2 with model-dependent statistical uncertainties inflated to realistic values that better reflect the combination of statistical and systematic uncertainty (Tayar et al. 2022), which we use for our

subsequent system analysis. We list the derived stellar parameters and uncertainties in Table 2.

## 4. Planet Characterization

### 4.1. Model Fit

We used the *exoplanet* Python package to simultaneously fit a model to the photometry and RV observations (Foreman-Mackey et al. 2020). The data input to our model were all Keck/HIRES RV observations reported in this work

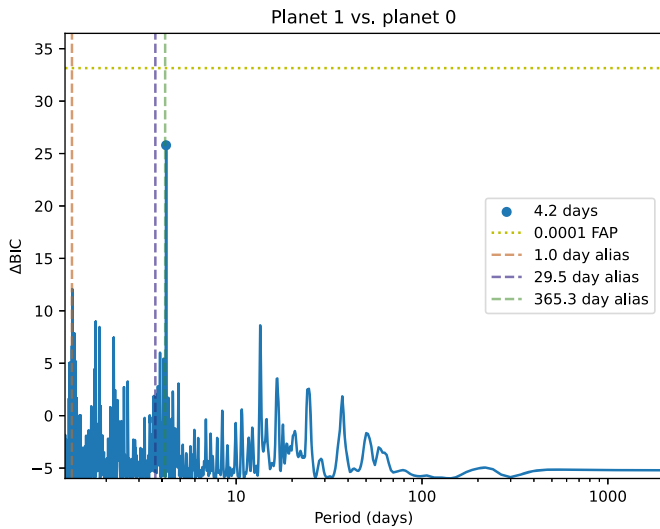


**Figure 4.** Periodogram of the Keck/HIRES RV measurements of TIC 365102760. The strongest signal present in the data, which does not correspond to a known alias of the Earth or Moon, is highlighted with a blue point. We find a power excess in the RV measurements at 4.2 days, with a  $\Delta\text{BIC} = 25.5$ , just below the false-alarm probability threshold of  $\Delta\text{BIC} = 33$  found to validate a planetary signal without additional information. This signal matches the period and phase of the signal found in the light curve of TIC 365102760.

**Table 1**

RVs and Uncertainties Measured for TIC 365102760 from Keck/HIRES

Time (JD—2457000)	Relative RV ( $\text{m s}^{-1}$ )
2379.061	$-0.8 \pm 1.4$
2386.098	$-8.9 \pm 1.5$
2396.065	$0.7 \pm 1.6$
2413.082	$6.2 \pm 1.7$
2421.011	$-3.5 \pm 2.1$
2423.062	$-3.1 \pm 1.5$
2435.909	$-3.2 \pm 1.4$
2442.078	$3.8 \pm 1.5$
2446.082	$0.1 \pm 1.7$
2449.040	$-2.2 \pm 1.6$
2503.884	$-15.7 \pm 1.6$
2509.902	$10.8 \pm 1.7$
2513.860	$7.4 \pm 1.6$
2545.776	$-7.5 \pm 1.9$
2655.144	$-8.0 \pm 1.6$
2657.138	$8.5 \pm 1.7$
2661.138	$7.7 \pm 1.6$
2712.088	$4.9 \pm 2.0$
2770.072	$3.0 \pm 1.6$
2772.008	$-4.0 \pm 1.4$

**Note.** The RVs have been sorted in time.

and a `giants` light curve made from all sectors of TESS FFI photometry available from the first 4 yr of the TESS mission. Our model used stellar parameters derived from our multi-wavelength photometric analysis following the procedure described above. We confirmed that this model was in strong agreement with an equivalent model fit using stellar parameters from `isoclassify` (Huber et al. 2017) with Gaia parallax, and input effective temperature ( $T_{\text{eff}}$ ) and metallicity estimated using `SpecMatch` (Petigura 2015) from spectral observations

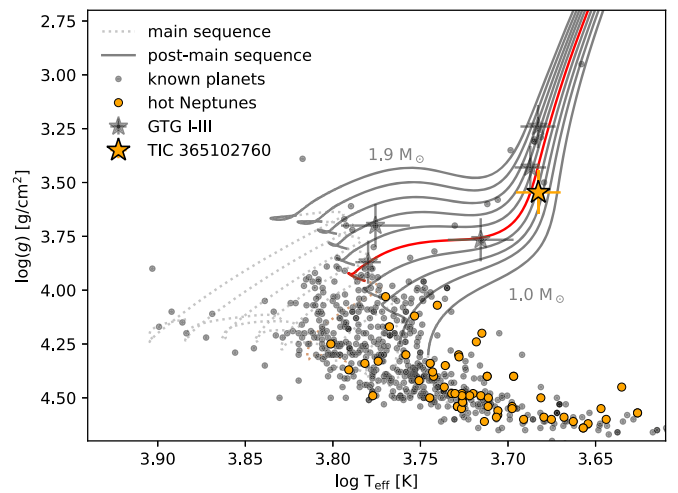


**Figure 5.** Surface gravity vs. effective temperature displayed logarithmically for TIC 365102760 along with the other planets discovered by the TESS GTG program (stars) compared to all known planets with well-characterized radii and masses (points). GTG discoveries have almost doubled the number of known systems on the subgiant and red giant branch. Hot Neptunes ( $3 R_{\oplus} < R_p < 8 R_{\oplus}$ ,  $P_{\text{orb}} < 10$  days) have been highlighted in orange. We also illustrate the MIST evolutionary tracks of  $1-2 M_{\odot}$ ,  $+0.25$  [Fe/H] dex stars in  $0.1 M_{\odot}$  increments for reference. We have highlighted a MIST evolutionary track for a  $1.4 M_{\odot}$ , [Fe/H] = 0.25 dex star in red, illustrating the rough evolutionary sequence probed by the GTG survey.

taken by the Keck/HIRES instrument. The photometric model input parameters used for our best-fit model can be found in Table 2.

Our initial choices of planet period and depth were taken from the BLS-search-determined values produced during the transit search described in Section 2.1 above. For limb darkening, we use the quadratic model prescribed by Kipping (2013) to provide a two-parameter model with uninformative sampling. We parameterized eccentricity using the single-planet eccentricity distribution of Van Eylen et al. (2019). We present our best-fit models to the light-curve and RV data for TIC 365102760 in Figure 7 and Table 3.

Given that the transit signal detected in the “KSP SAP,” “SAP FLUX,” and `eleanor` light curves does not match the period and phase of the RV data, we only fit for planet parameters of TIC 365102760 b using the `giants` and `SPOC` light curves. We note that the best exoplanet model fit using the `SPOC` light curve gives a radius of  $7.2 \pm 0.8 R_{\oplus}$ , in good agreement with the value determined using the `giants` light curve. We find that the RV signal for this planet is smaller than any other signal measured for a single transiting planet around an evolved star, but still constrains the planet mass to  $>3\sigma$ .

No significant out-of-transit variability can be resolved for TIC 365102760 b. Additional longer-baseline, higher-cadence data available for TIC 365102760 b from the extended TESS mission may provide evidence for variability in the stellar light curve that is currently not detectable. A long ( $\sim 90$  days) baseline of Kepler-like precision photometry should easily allow the detection of the asteroseismic signal of TIC 365102760 (Grunblatt et al. 2016, 2017). However, TIC 365102760 is expected to be too faint to allow asteroseismic detection with TESS (Huber et al. 2017, 2019). We have produced a power spectrum of our `giants` light curve but cannot identify any asteroseismic power excess in the data.

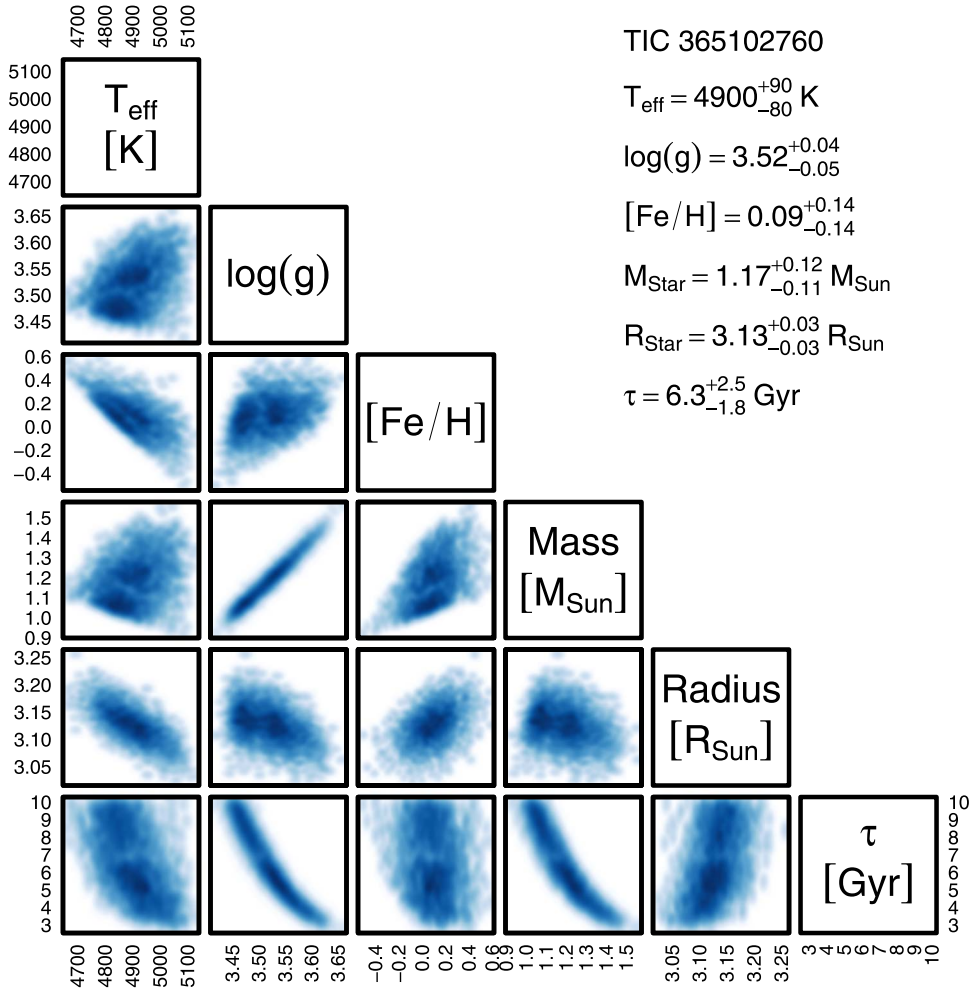


**Figure 6.** Corner plot illustrating the convergence of the stellar parameters determined for TIC 365102760 by fitting the Gaia DR2 *G*, 2MASS *J*, *H*, and *K*, and WISE *W1*, *W2*, and *W3* photometry as well as Gaia parallax to MIST isochrones. The stellar mass, radius, and age determined here are independently confirmed via a spectroscopic approach and are shown to agree with *isoclassify*-determined values within uncertainties.

### 5. Planet Irradiation, Potential Mass Loss, and Radius Inflation

We find that based on its mass, radius, and orbital period, TIC 365102760 b is a member of the relatively rare hot-Neptune planet population (Armstrong et al. 2020; Jenkins et al. 2020; Persson et al. 2022; Yoshida et al. 2023). Using the fitted values of  $19.2 \pm 4.2 M_{\oplus}$  and  $6.21 \pm 0.76 R_{\oplus}$  as the mass and radius for this planet, we determine a planet density of  $0.437^{+0.229}_{-0.150} \text{ g cm}^{-3}$ , among the lowest densities yet measured for a hot Neptune. We also use our constraints on stellar mass, metallicity, and luminosity, and we use the MIST evolutionary tracks (Choi et al. 2016) to determine the current incident flux and incident flux history of this planet, assuming the planet has not migrated since the star reached an age of 20 Myr. We find that this planet is the only hot Neptune ( $3\text{--}8 R_{\oplus}$ ,  $P < 10$  days) known in an evolved system (see Figure 5).

Given the low density and late evolutionary state of this system, we can use TIC 365102760 b to test existing photoevaporation and mass-loss prescriptions. We use previously established relations between the stellar bolometric flux and X-ray and ultraviolet (XUV) flux as a function of stellar age (King & Wheatley 2021) to estimate the current XUV flux and the XUV flux history of TIC 365102760 b. We show our

adopted XUV flux estimates as a function of time for the Sun and TIC 365102760 in Figure 8.

We use these XUV flux estimates to determine the instantaneous rates of mass loss from this planet over its lifetime using a modified version of the “energy-limited mass-loss” equation (Watson et al. 1981; Caldiroli et al. 2022):

$$\dot{M} = \eta_{\text{eff}} \frac{3F_{\text{XUV}}}{4KG\rho_p}, \quad (1)$$

where  $\dot{M}$  represents the planetary mass-loss rate,  $\eta_{\text{eff}}$  is the efficiency of the XUV evaporation from the planet,  $F_{\text{XUV}}$  is the stellar flux at high-energy, X-ray, and UV wavelengths,  $G$  is the gravitational constant, and  $\rho_p$  is the mean planetary density. We note that this mass-loss rate is likely an upper limit, as it applies primarily to pure hydrogen and helium-based atmospheres, an assumption that becomes less valid over time, as planet atmospheric metallicities increase due to fractionation and expose deeper atmospheric layers that may contain a mixture of gases with metallic species (Chen & Rogers 2016; Malsky & Rogers 2020). These metals contribute to cooling the outflow more efficiently, which in turn decreases mass-loss rates (Fossati et al. 2021). The correction factor  $K$  accounts for

**Table 2**

Stellar Properties Derived from a MIST Isochrone Fit to Multiwavelength Photometry from TESS, Gaia, 2MASS, and WISE Observations

Target ID	
TIC	365102760
2MASS	J20232153+5423395
Gaia DR2	2185044477033336064
<b>Observables</b>	
R.A. (J2015.5)	20:23:21.56
Decl. (J2015.5)	54:23:39.55
<i>B</i> mag	13.034 ± 0.526
<i>V</i> mag	12.154 ± 0.034
Gaia mag	11.9772 ± 0.0002
TESS mag	11.33 ± 0.01
2MASS <i>J</i> mag	10.406 ± 0.026
2MASS <i>H</i> mag	9.894 ± 0.032
2MASS <i>K</i> mag	9.788 ± 0.020
WISE W1 mag	9.721 ± 0.023
WISE W2 mag	9.813 ± 0.020
WISE W3 mag	9.700 ± 0.034
Proper Motion, R.A. $\mu_{R.A.}$	10.8797 ± 0.0418 mas yr <sup>-1</sup>
Proper Motion, decl. $\mu_{decl.}$	5.1928 ± 0.0422 mas yr <sup>-1</sup>
RV	-1.59 ± 0.25 km s <sup>-1</sup>
Distance	555.5 ± 7.6 pc
<b>Inferred Characteristics</b>	
Radius $R_*$	3.13 ± 0.12 $R_\odot$
Mass $M_*$	1.17 ± 0.12 $M_\odot$
$T_{eff}$	4900 ± 90 K
log( <i>g</i> )	3.52 ± 0.05 dex
[Fe/H]	0.09 ± 0.14 dex
Age	6.3 <sup>+2.5</sup> <sub>-1.8</sub> Gyr
Density $\rho_*$	0.041 ± 0.006 $\rho_\odot$

**Notes.** All parameters are in good agreement with an independent determination of stellar parameters using SpecMatch-derived parameters of Keck I/HIRES spectra with isoclassify.

the fact that atmospheric compounds only need to reach the planet’s Roche lobe radius to escape the planetary atmosphere (Erkaev et al. 2007):

$$K = 1 - \frac{3}{2} \left( \frac{R_p}{R_{Roche}} \right) + \frac{1}{2} \left( \frac{R_p}{R_{Roche}} \right)^3, \quad (2)$$

where, following the small planet-to-star mass ratio approximation, we approximate the Roche radius  $R_{Roche}$  as

$$R_{Roche} \approx a \left( \frac{M_p}{3M_*} \right)^{1/3}. \quad (3)$$

We estimate  $\eta_{eff}$  as a function of  $F_{XUV}$  at each time step, following the analytical approximation of Caldiroli et al. (2022), allowing us to determine instantaneous mass-loss rates  $\dot{M}$  for all of the planets in our sample. We then integrate these instantaneous mass-loss rates over the lifetimes of these planets using the bolometric flux values from the MIST stellar evolutionary tracks and the XUV-to-bolometric-flux relation as a function of age from King & Wheatley (2021) to determine the total mass lost by TIC 365102760 b over its lifetime. We then determine the ratio between the amount of mass lost and the current total mass of the planet, and compare this to the current planet mass relative to other known planetary systems, assuming planet formation and migration is complete after 20 Myr of stellar evolution. We compare the total mass lost as a

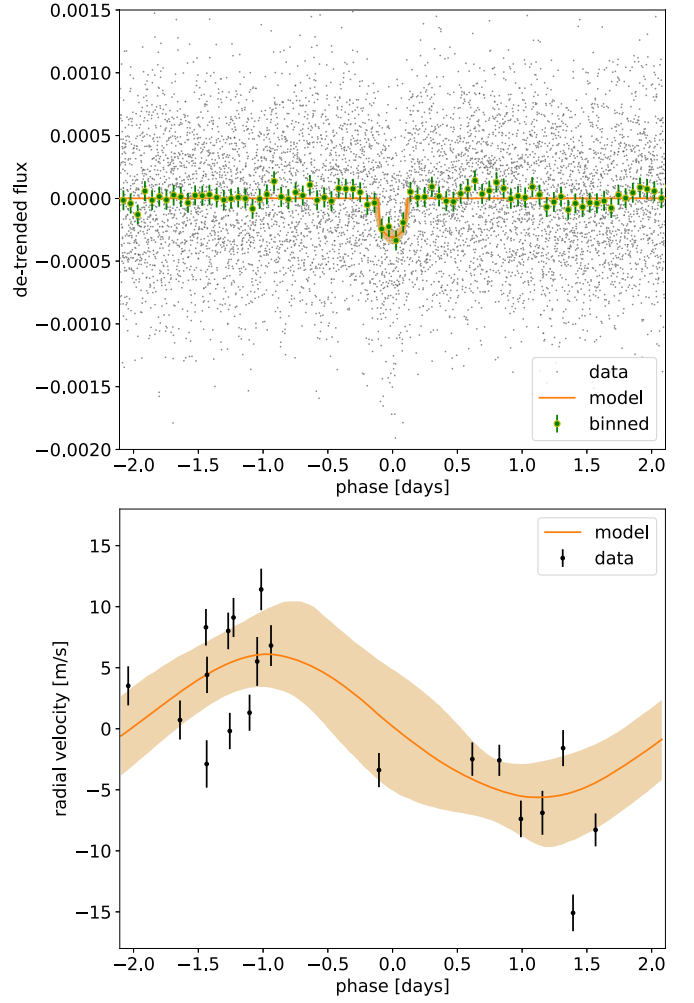


**Figure 7.** Top: the giants light curve of TIC 365102760 folded at a period of  $4.21285367 \pm 0.00000074$  days. The detrended photometry is shown in black, with the binned photometry plotted in green and the best-fit exoplanet model overplotted in orange, with 90% confidence intervals shaded. Bottom: all RV observations of TIC 365102760 (black) along with the best-fit exoplanet model and 90% confidence interval (orange) folded at the orbital period of the planet. Observations come from the Keck I/HIRES spectrograph on Maunakea.

function of planet radius for systems with ages and well-characterized planet masses and radii in Figure 9.

Using this formulation for atmospheric mass loss, we find that an upper limit of approximately 65% of the current planet mass, or  $\approx 12.5 M_\oplus$ , could have been lost over its lifetime (assuming that the planet radius has not changed over time), in good agreement with the fraction of mass loss inferred through an analytic approximation (Vissapragada et al. 2022b).

In order to confirm this cumulative atmospheric loss, we also determine the energy-limited mass-loss rate using a more simplified equation taken from (Watson et al. 1981):

$$\dot{M} = \frac{\varepsilon \pi R_{XUV}^2 F_{XUV}}{KGM_p/R_p}, \quad (4)$$

where  $\varepsilon$  represents an XUV heating efficiency (we conservatively assume 0.1; Shematovich et al. 2014; Salz et al. 2016),  $R_{XUV}$  is the effective absorption radius of the planet in XUV, and the other variables are the same as defined above. We assume an effective XUV absorption radius  $R_{XUV} = 1.1 R_p$ ,



**Table 3**  
Fit and Derived Parameters for TIC 365102760 b

Parameter	Prior	Value
<i>Transit Fit Parameters</i>		
Orbital period $P_{\text{orb}}$ (days)	$\log \mathcal{N}[4.2129, 0.001]$	$4.21285367 \pm 0.00000074$ day
Semimajor axis $a$ (au)	...	$0.0622 \pm 0.0049$
Transit epoch $t_0$ [BJD—2457000]	$\mathcal{N}[1684.177, 0.03]$	$2458684.146 \pm 0.011$
Transit duration $T_{\text{dur}}$ (hr)	...	$5.52^{+1.68}_{-0.72}$
Planet-to-star radius ratio $R_p/R_*$	...	$0.0176 \pm 0.0019$
Impact parameter $b$	$P_\beta(e \in [0, 1])^a$	$0.704 \pm 0.199$
Eccentricity $e$	Single-planet dist. from Van Eylen et al. (2019)	$< 0.406$
Argument of periastron $\Omega$	$\mathcal{U}[-\pi, \pi]$	$0.216 \pm 1.698$
Limb-darkening coefficient $q_1$	$[0, 2]^b$	$0.752 \pm 0.498$
Limb-darkening coefficient $q_2$	$[-1, 1]^b$	$-0.056 \pm 0.424$
<i>RV Fit Parameters</i>		
Semi-amplitude $K$ ( $\text{m s}^{-1}$ )	...	...
RV jitter $\sigma_{\text{RV}}$ ( $\text{m s}^{-1}$ )	$\mathcal{U}[0, 50]$	$7.4 \pm 1.6$
Offset $\gamma$ ( $\text{m s}^{-1}$ )	$\mathcal{U}[0, 10]$	$4.20 \pm 0.90$
Offset $\gamma$ ( $\text{m s}^{-1}$ )	$\mathcal{U}[-100, 100]$	$0.81 \pm 2.54$
<i>Derived Physical Parameters</i>		
Planet radius $R_p$	...	...
Planet mass $M_p$	$\mathcal{U}[0, 30]$	$6.21 \pm 0.76 R_\oplus$
Planet density $\rho_p$	$\mathcal{U}[0, 300]$	$19.2 \pm 4.2 M_\oplus$
$a/R_*$	...	$0.437^{+0.229}_{-0.156} \text{ g cm}^{-3}$
	...	$4.14 \pm 0.35$

**Notes.** Parameters without priors were inferred analytically through combinations of other parameters listed here.

<sup>a</sup> This parameterization is described by the beta distribution in Kipping (2013).

<sup>b</sup> Distributions follow the correlated two-parameter quadratic limb-darkening law from Kipping (2013).

based on previous estimates (Murray-Clay et al. 2009), which is likely an underestimate for this planet given its relatively low density and gravitational potential (Salz et al. 2016; Krenn et al. 2021). Using this more conservative approach, we determine a cumulative mass-loss fraction of 24% or total mass loss of 4.6  $M_\oplus$  for this planet. Through more sophisticated modeling that considers changes in planet radius due to both atmospheric inflation and mass loss simultaneously, we find a total amount of mass loss that falls between these two values (see Figure 10, described in detail at the end of this section).

Though the actual fraction of mass loss is difficult to estimate accurately (e.g., Pai Asnodkar et al. 2022), our predictions suggest that no currently known Neptune-sized planets are expected to have experienced higher fractional amounts of mass loss than TIC 365102760 b. Jupiter-sized planets are predicted to be more resilient to mass loss than Neptune-sized planets (Owen & Wu 2017; Caldiroli et al. 2022). Thus, perhaps unsurprisingly, no well-characterized planets larger than TIC 365102760 b with measured ages listed on the NASA Exoplanet Archive are expected to have undergone such a high fraction of atmospheric mass loss. Overall, only three well-characterized planets with measured ages are expected to have experienced more fractional mass loss than TIC 365102760 b (Frustagli et al. 2020; Weiss et al. 2021; Serrano et al. 2022). All of these planets are rocky, and thus any primordial atmosphere that might have existed has likely been stripped from them.

Models predict that  $\approx 20\%$ – $30\%$  of TIC 365102760 b’s mass should be contained in its gaseous envelope based on its incident flux, mass, and radius (Lopez & Fortney 2014; Chen & Rogers 2016). Thus, assuming that the planet did not experience migration or inflation after a system age of 20 Myr, most or all of the planet’s atmosphere should have been

stripped over its lifetime (Kubyskhina & Vidotto 2021; Kubyskhina & Fossati 2022). As the planet’s measured mass and radius imply it must have a gaseous envelope today, the planet may have a larger gas-to-core mass ratio than standard Neptune-mass planet models predict, resulting in a longer-lived atmosphere for this planet (Hallatt & Lee 2022). Such a large atmospheric mass would also imply a planetary metallicity and core mass lower than expected for a planet in this mass range (Thorngrén et al. 2016; Lee 2019). Thus, the origin and composition of this planet are currently unclear.

We consider some of the simplest scenarios by which TIC 365102760 b may have avoided such a high fraction of atmospheric mass loss here. First, the stellar flux in XUV may be significantly lower or absorbed less efficiently than existing models predict (Owen 2019; King & Wheatley 2021), preventing severe atmospheric erosion even if the planet has not changed its orbit or radius since formation. We note that we find a stellar spectral activity measure  $\log(R'_{\text{HK}}) = -5.4$  for our high-resolution spectroscopic observations of TIC 365102760, marginally lower than similar intermediate-mass, evolved planet host stars. XUV irradiation from an intermediate-mass star such as TIC 365102760 is expected to be over an order of magnitude stronger than the Sun, larger than the difference in XUV flux on the main sequence for the models used here, but the range in measured activity level for intermediate-mass main-sequence planet hosts spans more than an order of magnitude (Fossati et al. 2018; France et al. 2018). Correlations between stellar activity levels and the expected atmospheric erosion of other planets could help to validate this hypothesis. Mass loss could also be less efficient than models predict in this planet due to metal line cooling (Owen & Jackson 2012), magnetic suppression (Owen & Adams 2014), or suppression via stellar winds (Wang & Dai 2021).

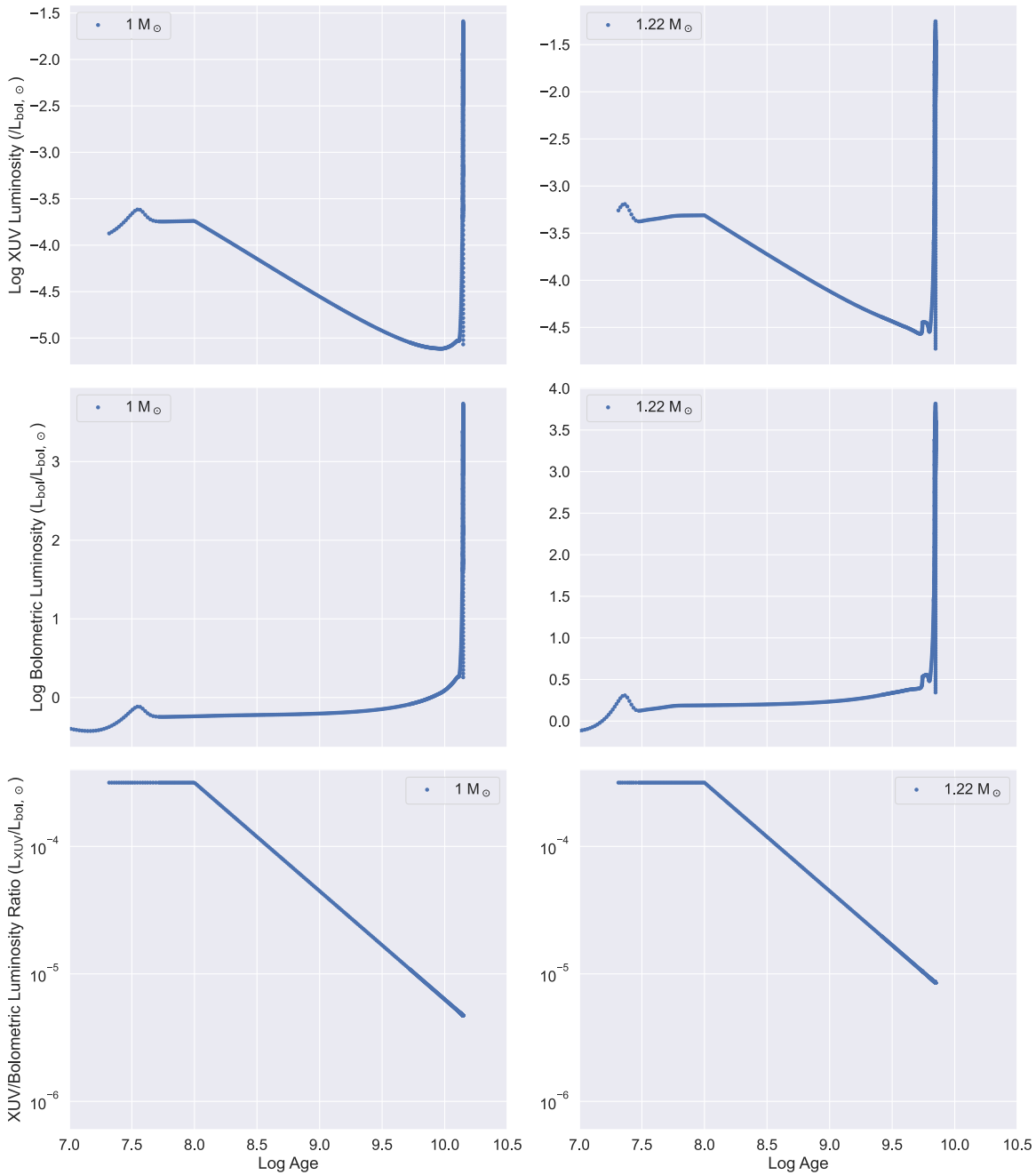


**Figure 8.** Top row: XUV luminosity vs. the logarithm of the stellar age in years for  $1 M_{\odot}$  (left) and  $1.22 M_{\odot}$  (right) stellar models. The XUV luminosity is defined with respect to the bolometric luminosity of the Sun and is only modeled from 20 Myr after star formation to the end of the red giant branch phase of stellar evolution. Middle row: bolometric luminosity for  $1 M_{\odot}$  (left) and  $1.22 M_{\odot}$  (right) stellar models, also defined with respect to the bolometric luminosity of the Sun. Bottom row: ratio of XUV flux to bolometric flux as a function of age for  $1 M_{\odot}$  (left) and  $1.22 M_{\odot}$  (right) stellar models.

Second, the planet may have migrated to its current orbit during the main-sequence lifetime of its host star from a previous larger orbit, avoiding the highest intensity of XUV irradiation from its host star. Both star–planet and planet–planet interactions could result in orbit reconfiguration. However, the absence of any transit timing variations, astrometric noise (Gaia Collaboration et al. 2018), or additional RV signal or trend suggests that there are no other planets relatively near to TIC 365102760 b in this system, suggesting that recent planet–planet interactions are not likely. Furthermore, TIC 365102760 b does not appear to have a high-eccentricity orbit, suggesting that migration due to star–planet interaction is also unlikely or

not very recent in the system’s history (Villaver et al. 2014). Better constraints on the eccentricity via additional RV follow-up or constraint of the obliquity of the planetary orbit relative to the stellar spin axis could also support or refute evidence for orbital migration (Bourrier et al. 2023).

Finally, the planet may have been significantly smaller in the past, limiting the instantaneous rate of mass loss on the main sequence. Our estimates of cumulative mass loss assume no change in planet radius as a function of time, which is not expected for planets in this mass and temperature regime experiencing significant mass loss (Thorngren et al. 2023). Atmospheric mass loss tends to shrink planets over time in this

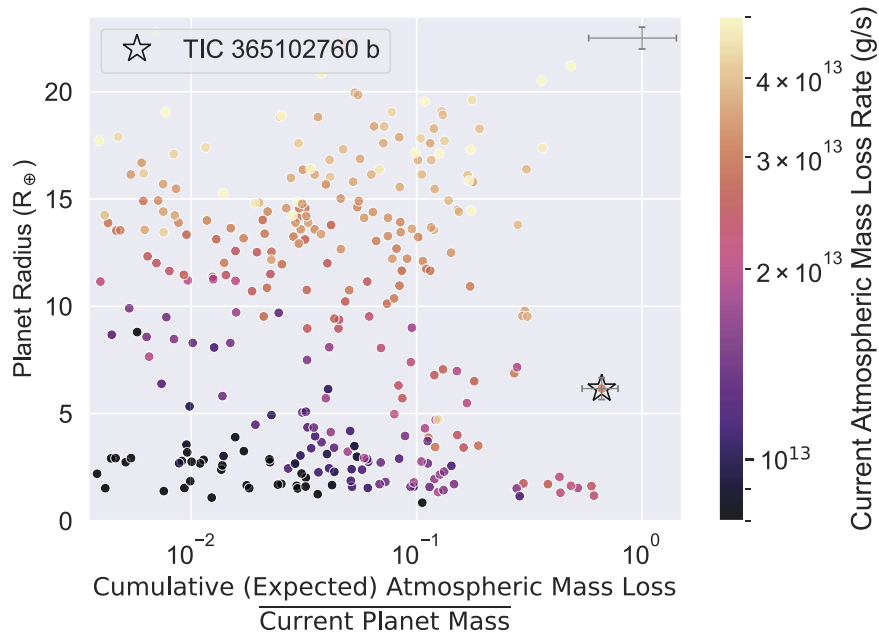


**Figure 9.** Planet radius vs. the fraction of estimated total atmospheric mass loss divided by the current planet mass for all planets with masses and radii reported with  $\geq 50\%$  accuracy, with ages from the NASA Exoplanet Archive accessed on 2023 January 31. The color indicates the atmospheric mass-loss rate in grams per second. Evolved planets have been highlighted with stars, where TIC 365102760 b is indicated by the largest star. The average errors are illustrated in the upper right-hand corner of the figure. TIC 365102760 b both has a higher current mass-loss rate and is predicted to have experienced more atmospheric mass loss than all other gaseous planets, with only a few rocky planets experiencing higher rates of mass loss. As the atmospheric mass for this planet is predicted to be smaller than the total mass expected to have been lost, it is unclear how TIC 365102760 b has retained an atmosphere given its current radius and orbit around its host star.

mass and temperature regime, generally resulting in more mass loss than what we assume in Figure 9. However, if we assume the recent increase in irradiation received by this planet due to post-main-sequence evolution could have resulted in the rapid re-inflation of this planet (Thorngren et al. 2021), this implies a smaller radius for the planet when TIC 365102760 was on the main sequence.

Following the formulation of Thorngren et al. (2021) and assuming a late-stage inflation efficiency comparable to what has been observed in other systems (Grunblatt et al. 2017), we can model changes in the radius of TIC 365102760 b over the lifetime of the system. We compare this to an atmospheric mass-loss model of the planet radius following Thorngren et al. (2023), tuned such that we recover the measured mass and radius for the planet at the current system age. We show the expected radius evolution as a function of time for both of these scenarios using the observed planet mass, radius, and age in Figure 10. We note that at 1 Gyr, the inflated planet model radius is  $\approx 16\%$  smaller than the current radius, while the atmospheric mass-loss model radius is  $\approx 5\%$  larger. As the atmospheric mass-loss rate depends on the density of the planet, this implies a  $\sim 40\%$  reduction in instantaneous mass loss at that time for the late-stage inflation model relative to the atmospheric mass-loss model. Since stellar XUV irradiation is maximized at ages of 1 Gyr or less, this results in a similar  $\sim 40\%$  reduction of the total atmospheric mass loss of the planet if it has inflated during post-main-sequence evolution.

In order to ensure that photoevaporation is the dominant mass-loss process occurring in this system, we also calculate the Roche lobe size for all planets in this sample. We find that very few well-characterized planets have radii that reach more than half their Roche lobe and no planets fill more than 60% of their Roche lobe in our analysis. TIC 365102760 b appears to

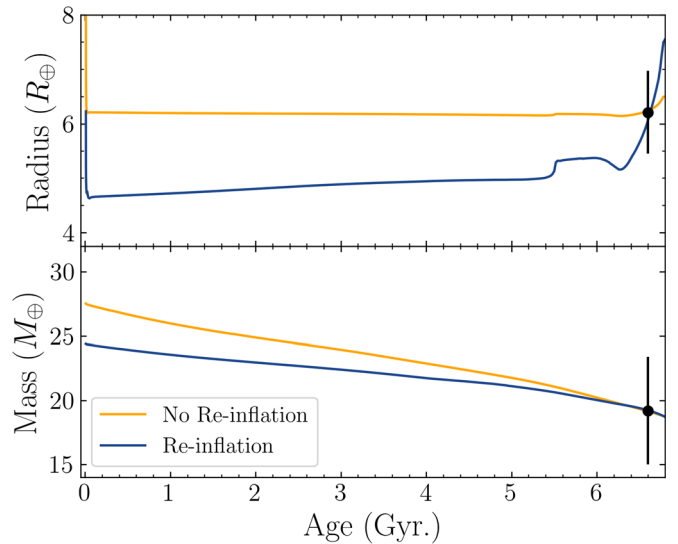


**Figure 10.** Planet radius vs. age for two toy models of TIC 365102760 b that agree with the median mass, radius, age, and flux measured here (black points). A planet model following the rapid re-inflation formulation of Thorngren et al. (2021) is shown in blue, while an atmospheric mass-loss model following the formulation of Thorngren et al. (2023), tuned such that we recover the measured planet mass and radius at the current system age, is shown in orange. This rapid re-inflation model implies the planet was smaller during the main-sequence phase, resulting in a  $\sim 40\%$  reduction in total atmospheric mass loss from TIC 365102760 b relative to models that do not allow late-stage inflation.

fill only 20% of its Roche lobe and thus is unlikely to be experiencing Roche lobe overflow. This is in line with Jackson et al. (2017) and Koskinen et al. (2022), indicating that Roche lobe overflow tends only to be important for hot Neptunes with  $\lesssim 2$  days orbital periods.

## 6. Potential Follow-up Observations

### 6.1. Transit Spectroscopy

Little is understood about the evolution of planetary atmospheres over time, and few observations of planetary atmospheres have been conducted for planets orbiting evolved stars (Kilpatrick et al. 2018; Colón et al. 2020; Mounzer et al. 2022). Due to their particularly short orbits, the system introduced here is more well suited for atmospheric characterization than other planets orbiting evolved stars.

Future observations with facilities capable of higher-precision photometry will confirm the true transit depth of this system, more precisely constraining the radius of TIC 365102760 b. Observations of the planet transit using a ground-based telescope with diffuser-assisted photometry (Stefansson et al. 2017) may also provide the requisite signal-to-noise ratio to obtain a more precise transit depth of TIC 365102760 b. Given the high scatter and low signal-to-noise ratio of this transit, planet parameters could also be significantly improved with transit observations taken by JWST (Gardner et al. 2006). The higher photometric precision of JWST relative to TESS will allow better constraints on the planet radius, as well as transit shape and duration, which will help to constrain planetary orbit properties. Furthermore, the wavelength sensitivity of JWST may allow transmission spectroscopy. We find that TIC 365102760 b has a transmission spectroscopy metric (Kempton et al. 2018) value of  $\sim 25$ , similar to the temperate sub-Neptune K2-18 b, which was observed by JWST in 2023 (Madhusudhan et al. 2023), making this planet a challenging but accessible target for JWST transit spectroscopy observations. Preliminary predictions and comparisons to similar targets suggest that atomic and/or molecular signatures, clouds, and/or hazes should be detectable in the planet’s atmosphere (Mounzer et al. 2022; Rustamkulov et al. 2023). Recent observations have suggested a distinction in the atmospheric profiles of hot and ultrahot Jupiters (Baxter et al. 2021), which may also be seen between this planet and slightly cooler hot Neptunes. Additionally, the constraint of the overall metallicity of the planet’s atmosphere could constrain the planet’s initial mass and gas-to-core mass ratio (Hallatt & Lee 2022). Atomic and molecular abundances measured from transmission spectroscopy can probe where the planet originally formed and at what point in its lifetime it moved to its current orbit (Öberg et al. 2011; Dawson & Johnson 2018).

### 6.2. Radial Velocity

Additional RV observations of this system will also test dynamical evolution models. Grunblatt et al. (2018) showed that giant planets orbiting giant stars at periods  $< 30$  days have average eccentricities  $e > 0.1$ . However, at the shortest orbital periods ( $< 5$  days), even planets around evolved stars appear to have largely circular orbits. Constraints on orbital eccentricities will constrain both planet engulfment and stellar structure models (Weinberg et al. 2017; Sun et al. 2018; Soares-Furtado et al. 2021; Grunblatt et al. 2023; Weinberg et al. 2024). We find no evidence for significant eccentricity in the orbit of TIC 365102760 b based on our current set of observations. Using our best-fit exoplanet model of this system, we find that TIC 365102760 b has an eccentricity of 0.4 or less at  $2\sigma$  significance. A more finely sampled set of RV measurements for this target with next-generation instrumentation, such as the Keck Planet Finder (KPF; Gibson et al. 2016) or WIYN/NEID

(Schwab et al. 2016), will place tighter constraints on the planet’s eccentricity and thus inform models of tidal evolution for the lowest-mass-ratio planetary systems and determine whether this planet has completed any potential high-eccentricity migration (Villaver et al. 2014).

The RV jitter of TIC 365102760 is measured to be  $4.20 \pm 0.90 \text{ m s}^{-1}$ , in agreement with the  $5 \text{ m s}^{-1}$  jitter typically expected for stars at this evolutionary state (Tayar et al. 2019). Low RV jitter may be related to lower stellar activity, which is likely also correlated with lower XUV flux for a star (Chadney et al. 2015). Further RV follow-up of this system with next-generation extreme-precision RV instruments such as NEID and KPF may help to distinguish between stellar jitter and planetary signal in this system, improving our ability to characterize this planet as well as its host star.

## 7. Is TIC 365102760 b Experiencing Runaway Inspiral?

The expected tidal interaction between hot gas-giant planets and evolved host stars is expected to result in rapid orbital decay and the eventual engulfment of the planet. However, orbital decay has only been measured in two systems to date, WASP-12 b and Kepler-1658 b (Patra et al. 2020; Yee et al. 2020; Turner et al. 2021; Vissapragada et al. 2022a), both of which were less evolved than the system studied here. By constraining the rate of orbital decay in evolved systems, we can better characterize the strength of star–planet tidal interactions and their dependence on star and planet properties.

Figure 11 illustrates the population of known planets, highlighting those planets that are most likely to be experiencing strong orbital decay, as well as the decay rates predicted using the prescription from Goldreich & Soter (1966), assuming a modified stellar tidal quality factor  $Q'_* = 10^6$ . The planets with the smallest relative orbital separations and highest masses relative to their stars decay most quickly and can be found in the upper left-hand corner of this plot. We have illustrated the new planets found by this survey as squares on this plot. These planets are among the best candidates for detecting orbital decay. In particular, TIC 365102760 b is predicted to have the most rapidly decaying orbit for a known planetary system with a mass ratio below  $10^{-4}$  to date. In addition, TIC 365102760 b also orbits a relatively cool star, which is expected to increase the speed of its orbital decay due to more rapid tidal dissipation in TIC 365102760’s thick outer convective envelope (Patra et al. 2020). However, the relatively noisy TESS coverage for this system and relatively slow predicted orbital decay rate of this planet make it unlikely that orbital decay will be detectable for this system in the next decade.

To predict the orbital stability of this system at the current time, we use the formulation of Sun et al. (2018) to determine the critical semimajor axis,  $a_{\text{crit}}$ , at which the dynamical tides are expected to overcome equilibrium tides and begin the process of runaway inspiral. We compare  $a_{\text{crit}}$  to the current semimajor axis  $a$  of the system, which we have determined to be  $0.062 \pm 0.005 \text{ au}$ . Following the analytical approximations for  $a_{\text{crit}}$  assuming various rates of tidal dissipation, which allow for different eddy sizes and turnover times within the convective envelope of the star, we determine a maximum  $a_{\text{crit}} = 0.055 \text{ au}$  for this system, assuming a nonreduced kinematic viscosity for this star (Zahn 1977). Thus, this planet is not predicted to be experiencing runaway inspiral and orbital

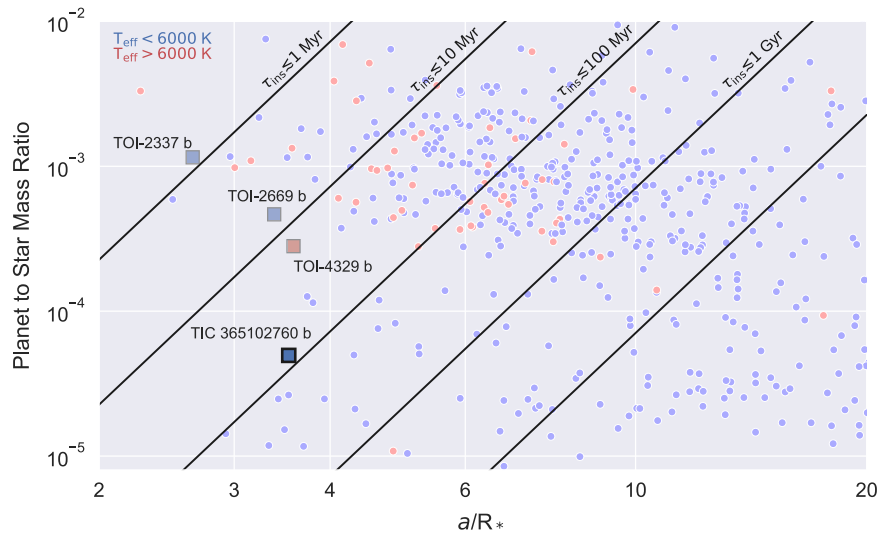


**Figure 11.** Semimajor axis divided by stellar radius vs. planet-to-star mass ratio for confirmed planets. The orbital decay timescales are determined assuming a tidal decrease toward the upper left of this plot, where the black diagonals correspond to theorized rates of orbital decay, with the leftmost line corresponding to a decay timescale of  $10^6$  yr and each following line increasing by a factor of 10. The blue points have stellar effective temperatures  $< 6000$  K, as reported by the NASA Exoplanet Archive, while the red points represent planets around hotter stars. The planets confirmed by our second TESS GTG paper (Grunblatt et al. 2022) are shown as squares with black outlines and are populating relatively sparse regions of parameter space on this plot that correspond to rapid orbital decay. TIC 365102760 b may be experiencing the fastest rate of orbital decay of any planetary system known with a mass ratio below  $10^{-4}$  or a planet mass  $< 25 M_{\oplus}$ .

decay at this time, suggesting that the host star must grow significantly in radius before this process begins.

## 8. Conclusions

Our search for planets transiting evolved stars using TESS FFI data has led to the discovery of TIC 365102760 b, the lowest-mass planet found orbiting an evolved star ( $R_* > 2 R_{\odot}$ ,  $T_{\text{eff}} < 6000$  K) to date. This planet will serve as a benchmark for understanding late-stage low-mass planet evolution. Our main conclusions are as follows:

1. TIC 365102760 b is an inflated, hot-Neptune-like planet and among the smallest and lowest-mass planets ever confirmed to be transiting a red giant star. Despite its low mass and high incident flux, the planet appears to be holding onto a significant atmosphere. This suggests that it has a relatively high mass fraction of hydrogen and helium.
2. While there are multiple scenarios that may allow the planet to retain its atmosphere in its current configuration, assuming that the planet has been reinflated during post-main-sequence evolution allows the planet to retain a significantly larger fraction of its atmosphere when undergoing atmospheric mass loss during its main-sequence lifetime.
3. The temperature and radius currently observed for this planet place constraints on the allowed efficiency of re-inflation processes in the lowest-mass planets and suggest that this planet is experiencing different atmospheric phenomena than hot Neptunes around main-sequence stars.
4. Though this planet will not survive at its current orbit for much longer around its red giant host, it is unlikely to be experiencing runaway orbital inspiral at this time. The planet is expected to survive  $< 100$  Myr before beginning the inspiral process, assuming it does not lose a significant amount of its mass over that time. This is

one of the shortest inspiral timescales for Neptune-mass planets.

The discovery of a low-density hot Neptune orbiting an evolved star demonstrates that the atmospheres of these planets are more resilient than previously thought. Furthermore, it demonstrates that planets that are smaller than Jupiter in size may be inflated directly by irradiation from their host stars. This has important implications for understanding the structure and evolution of Neptune-sized planets and interpreting the demographics of the known planet population. Finding more evolved, hot, Neptune-sized planets at different masses and densities may reveal additional trends with planet composition or stellar activity. Focused searches for these evolved systems are necessary, as these planets are missed by general searches for transiting planets (e.g., Grunblatt et al. 2023).

Additional observations of TIC 365102760 b using ground-based and space-based spectroscopic approaches may reveal atmospheric outflows from this planet, better constraining the lifetime of its atmosphere as well as its atmospheric composition. An extended atmosphere potentially indicative of outflow has already been detected via sodium D line transmission in another evolved, inflated planet, KELT-11 b (Mounzer et al. 2022), though at levels lower than initially expected. This may be due to high-altitude clouds, which may be related to silicate cloud production resulting from rapid planet re-inflation (Gao et al. 2020; Thorngren et al. 2021). Constraining the balance between planet atmospheric inflation and mass loss will help reveal the evolution of planetary atmospheres over time, clarifying planet demographic features such as the hot-Neptune desert.




## Acknowledgments












We acknowledge the use of public TESS data from pipelines at the TESS Science Office and at the TESS Science Processing Operations Center. Resources supporting this work were provided by the NASA High-End Computing (HEC) Program through the NASA Advanced Supercomputing (NAS) Division

at Ames Research Center for the production of the SPOC data products. This work was supported by a NASA Keck PI Data Award, administered by the NASA Exoplanet Science Institute. Data presented herein were obtained at the W. M. Keck Observatory from telescope time allocated to the National Aeronautics and Space Administration through the agency's scientific partnership with the California Institute of Technology and the University of California. The Observatory was made possible by the generous financial support of the W. M. Keck Foundation. The authors wish to recognize and acknowledge the very significant cultural role and reverence that the summit of Maunakea has always had within the indigenous Hawaiian community. We are most fortunate to have the opportunity to conduct observations from this mountain. S.G. acknowledges support by the National Aeronautics and Space Administration under grants 80NSSC23K0137 and 80NSSC23K0168. S.G., N.S., and D.H. acknowledge support by the National Aeronautics and Space Administration under grant 80NSSC19K0593 issued through the TESS Guest Investigator Program. S.G. and K.S. acknowledge support by the National Aeronautics and Space Administration under grant 80NSSC20K0059 issued through the TESS Guest Investigator Program. D.H. acknowledges support from the Alfred P. Sloan Foundation and the National Aeronautics and Space Administration (80NSSC21K0652) and from the National Science Foundation (80NSSC21K0652). N.S. acknowledges support from the National Science Foundation through the Graduate Research Fellowship Program under grants 1842402 and DGE-1752134. Any opinions, findings, and conclusions or recommendations expressed in this material are those of the authors and do not necessarily reflect the views of the National Science Foundation. This research has made use of the Exoplanet Follow-up Observation Program website, which is operated by the California Institute of Technology under contract with the National Aeronautics and Space Administration under the Exoplanet Exploration Program. Funding for the TESS mission is provided by NASA's Science Mission Directorate.

*Software:* this work has relied heavily on open-source software tools, and we would like to thank the developers for their contributions to the astronomy community. For data access and detrending, this research made use of *lightkurve*, a Python package for Kepler and TESS data analysis (Lightkurve Collaboration et al. 2018); *TESSCut*, a MAST tool for extracting observations from TESS FFIs (Brasseur et al. 2019); and the MIT QLP, a pipeline for producing and detrending TESS FFI light curves (Kunimoto et al. 2021). The analysis portion of this research relied on *astropy* (Astropy Collaboration et al. 2013; Price-Whelan et al. 2018), as well as *exoplanet* (Foreman-Mackey et al. 2020) and its dependencies (Kipping 2013; Salvatier et al. 2016; Theano Development Team 2016; Agol et al. 2019; Luger et al. 2019; Foreman-Mackey et al. 2020).

### ORCID iDs

Samuel K. Grunblatt  <https://orcid.org/0000-0003-4976-9980>  
 Nicholas Saunders  <https://orcid.org/0000-0003-2657-3889>  
 Daniel Huber  <https://orcid.org/0000-0001-8832-4488>  
 Daniel Thorngren  <https://orcid.org/0000-0002-5113-8558>  
 Shreyas Vissapragada  <https://orcid.org/0000-0003-2527-1475>  
 Stephanie Yoshida  <https://orcid.org/0000-0003-4015-9975>

Kevin C. Schlaufman  <https://orcid.org/0000-0001-5761-6779>  
 Steven Giacalone  <https://orcid.org/0000-0002-8965-3969>  
 Mason Macdougall  <https://orcid.org/0000-0003-2562-9043>  
 Ashley Chontos  <https://orcid.org/0000-0003-1125-2564>  
 Emma Turtelboom  <https://orcid.org/0000-0002-1845-2617>  
 Corey Beard  <https://orcid.org/0000-0001-7708-2364>  
 Joseph M. Akana Murphy  <https://orcid.org/0000-0001-8898-8284>  
 Malena Rice  <https://orcid.org/0000-0002-7670-670X>  
 Howard Isaacson  <https://orcid.org/0000-0002-0531-1073>  
 Ruth Angus  <https://orcid.org/0000-0003-4540-5661>  
 Andrew W. Howard  <https://orcid.org/0000-0001-8638-0320>

### References

- Agol, E., Luger, R., & Foreman-Mackey, D. 2019, *AJ*, 159, 123  
 Arenou, F., Luri, X., Babusiaux, C., et al. 2018, *A&A*, 616, A17  
 Armstrong, D. J., Lopez, T. A., Adibekyan, V., et al. 2020, *Natur*, 583, 39  
 Astropy Collaboration, Robitaille, T. P., Tollerud, E. J., et al. 2013, *A&A*, 558, A33  
 Bailer-Jones, C. A. L., Rybizki, J., Foesneau, M., Demleitner, M., & Andrae, R. 2021, *AJ*, 161, 147  
 Barker, A. J. 2020, *MNRAS*, 498, 2270  
 Baxter, C., Désert, J.-M., Tsai, S.-M., et al. 2021, *A&A*, 648, A127  
 Berger, T. A., Huber, D., Gaidos, E., van Saders, J. L., & Weiss, L. M. 2020, *AJ*, 160, 108  
 Bourrier, V., Attia, O., Mallonn, M., et al. 2023, *A&A*, 669, A63  
 Brasseur, C. E., Phillip, C., Fleming, S. W., Mullally, S. E., & White, R. L., 2019 *Astrocute: Tools for Creating Cutouts of TESS Images*, Astrophysics Source Code Library, ascl:1905.007  
 Caldiroli, A., Haardt, F., Gallo, E., et al. 2022, *A&A*, 663, A122  
 Chadney, J. M., Galand, M., Unruh, Y. C., Koskinen, T. T., & Sanz-Forcada, J. 2015, *Icar*, 250, 357  
 Chen, H., & Rogers, L. A. 2016, *ApJ*, 831, 180  
 Choi, J., Dotter, A., Conroy, C., et al. 2016, *ApJ*, 823, 102  
 Colón, K. D., Kreidberg, L., Welbanks, L., et al. 2020, *AJ*, 160, 280  
 Dawson, R. I., & Johnson, J. A. 2018, *ARA&A*, 56, 175  
 Dewberry, J. W., & Wu, S. C. 2024, *MNRAS*, 527, 2288  
 Dotter, A. 2016, *ApJS*, 222, 8  
 El-Badry, K., Rix, H.-W., & Heintz, T. M. 2021, *MNRAS*, 506, 2269  
 Erkaev, N. V., Kulikov, Y. N., Lammer, H., et al. 2007, *A&A*, 472, 329  
 Evans, D. W., Riello, M., De Angeli, F., et al. 2018, *A&A*, 616, A4  
 Fabricius, C., Luri, X., Arenou, F., et al. 2021, *A&A*, 649, A5  
 Feinstein, A. D., Montet, B. T., Foreman-Mackey, D., et al. 2019, *PASP*, 131, 094502  
 Feroz, F., & Hobson, M. P. 2008, *MNRAS*, 384, 449  
 Feroz, F., Hobson, M. P., & Bridges, M. 2009, *MNRAS*, 398, 1601  
 Feroz, F., Hobson, M. P., Cameron, E., & Pettitt, A. N. 2019, *OJAp*, 2, 10  
 Foreman-Mackey, D., Luger, R., Czekala, I., et al. 2020, *exoplanet-dev/exoplanet v0.3.2*, Zenodo, doi:10.5281/zenodo.1998447  
 Fossati, L., Koskinen, T., Lothringer, J. D., et al. 2018, *ApJL*, 868, L30  
 Fossati, L., Young, M. E., Shulyak, D., et al. 2021, *A&A*, 653, A52  
 France, K., Arulanantham, N., Fossati, L., et al. 2018, *ApJS*, 239, 16  
 Frustagli, G., Poretti, E., Milbourne, T., et al. 2020, *A&A*, 633, A133  
 Gaia Collaboration, Brown, A. G. A., Vallenari, A., et al. 2018, *A&A*, 616, A1  
 Gaia Collaboration, Brown, A. G. A., Vallenari, A., et al. 2021, *A&A*, 649, A1  
 Gaia Collaboration, Prusti, T., de Bruijne, J. H. J., et al. 2016, *A&A*, 595, A1  
 Gao, P., Thorngren, D. P., Lee, E. K. H., et al. 2020, *NatAs*, 4, 951  
 Gardner, J. P., Mather, J. C., Clampin, M., et al. 2006, *SSRv*, 123, 485  
 Gibson, S. R., Howard, A. W., Marcy, G. W., et al. 2016, *Proc. SPIE*, 9908, 990870  
 Goldreich, P., & Soter, S. 1966, *Icar*, 5, 375  
 Green, G. M., Schlafly, E., Zucker, C., Speagle, J. S., & Finkbeiner, D. 2019, *ApJ*, 887, 93  
 Green, G. M., Schlafly, E. F., Finkbeiner, D. P., et al. 2014, *ApJ*, 783, 114  
 Grunblatt, S. K., Huber, D., Gaidos, E., et al. 2017, *AJ*, 154, 254  
 Grunblatt, S. K., Huber, D., Gaidos, E., et al. 2018, *ApJL*, 861, L5  
 Grunblatt, S. K., Huber, D., Gaidos, E., et al. 2019, *AJ*, 158, 227  
 Grunblatt, S. K., Huber, D., Gaidos, E. J., et al. 2016, *AJ*, 152, 185  
 Grunblatt, S. K., Saunders, N., Chontos, A., et al. 2023, *AJ*, 165, 44  
 Grunblatt, S. K., Saunders, N., Sun, M., et al. 2022, *AJ*, 163, 120

- Guerrero, N. M., Seager, S., Huang, C. X., et al. 2021, *ApJS*, **254**, 39
- Guillot, T., Burrows, A., Hubbard, W. B., Lunine, J. I., & Saumon, D. 1996, *ApJL*, **459**, L35
- Hallatt, T., & Lee, E. J. 2022, *ApJ*, **924**, 9
- Hamer, J. H., & Schlaufman, K. C. 2019, *AJ*, **158**, 190
- Huber, D., Chaplin, W. J., Chontos, A., et al. 2019, *AJ*, **157**, 245
- Huber, D., Zinn, J., Bojsen-Hansen, M., et al. 2017, *ApJ*, **844**, 102
- Jackson, B., Arras, P., Penev, K., Peacock, S., & Marchant, P. 2017, *ApJ*, **835**, 145
- Jenkins, J. M., Caldwell, D. A., Chandrasekaran, H., et al. 2010, *ApJL*, **713**, L87
- Jenkins, J. M., Twicken, J. D., McCauliff, S., et al. 2016, *Proc. SPIE*, **9913**, 99133E
- Jenkins, J. S., Díaz, M. R., Kurtovic, N. T., et al. 2020, *NatAs*, **4**, 1148
- Jermyn, A. S., Bauer, E. B., Schwab, J., et al. 2023, *ApJS*, **265**, 15
- Johnson, J. A., Aller, K. M., Howard, A. W., & Crepp, J. R. 2010, *PASP*, **122**, 905
- Johnson, J. A., Fischer, D. A., Marcy, G. W., et al. 2007, *ApJ*, **665**, 785
- Kempton, E. M. R., Bean, J. L., Louie, D. R., et al. 2018, *PASP*, **130**, 114401
- Kilpatrick, B. M., Cubillos, P. E., Stevenson, K. B., et al. 2018, *AJ*, **156**, 103
- King, G. W., & Wheatley, P. J. 2021, *MNRAS*, **501**, L28
- Kipping, D. M. 2013, *MNRAS*, **435**, 2152
- Kipping, D. M. 2013, *MNRAS: Letters*, **434**, L51
- Koskinen, T. T., Lavvas, P., Huang, C., et al. 2022, *ApJ*, **929**, 52
- Kovács, G., Zucker, S., & Mazeh, T. 2002, *A&A*, **391**, 369
- Krenn, A. F., Fossati, L., Kubyskhina, D., & Lammer, H. 2021, *A&A*, **650**, A94
- Kubyskhina, D., & Fossati, L. 2022, *A&A*, **668**, A178
- Kubyskhina, D., & Vidotto, A. A. 2021, *MNRAS*, **504**, 2034
- Kunimoto, M., Huang, C., Tey, E., et al. 2021, *RNAAS*, **5**, 234
- Lee, E. J. 2019, *ApJ*, **878**, 36
- Lightkurve Collaboration, Cardoso, J. V. d. M., Hedges, C., et al., 2018  
Lightkurve: Kepler and TESS time Series Analysis in Python, Astrophysics  
Source Code Library, ascl:[1812.013](https://www.aanda.org/abstract/201812013)
- Lindgren, L., Bastian, U., Biermann, M., et al. 2021a, *A&A*, **649**, A4
- Lindgren, L., Klioner, S. A., Hernández, J., et al. 2021b, *A&A*, **649**, A2
- Lopez, E. D., & Fortney, J. J. 2014, *ApJ*, **792**, 1
- Luger, R., Agol, E., Foreman-Mackey, D., et al. 2019, *AJ*, **157**, 64
- Madhusudhan, N., Sarkar, S., Constantinou, S., et al. 2023, *ApJL*, **956**, L13
- Mainzer, A., Bauer, J., Grav, T., et al. 2011, *ApJ*, **731**, 53
- Malsky, I., & Rogers, L. A. 2020, *ApJ*, **896**, 48
- Matsakos, T., & Königl, A. 2016, *ApJL*, **820**, L8
- Mazeh, T., Holczer, T., & Faigler, S. 2016, *A&A*, **589**, A75
- Morton, T. D., 2015 isochrones: Stellar model grid package, Astrophysics  
Source Code Library, ascl:[1503.010](https://www.aanda.org/abstract/201503010)
- Mounzer, D., Lovis, C., Seidel, J. V., et al. 2022, *A&A*, **668**, A1
- Murray-Clay, R. A., Chiang, E. I., & Murray, N. 2009, *ApJ*, **693**, 23
- Öberg, K. I., Murray-Clay, R., & Bergin, E. A. 2011, *ApJL*, **743**, L16
- Ogilvie, G. I. 2014, *ARA&A*, **52**, 171
- Owen, J. E. 2019, *AREPS*, **47**, 67
- Owen, J. E., & Adams, F. C. 2014, *MNRAS*, **444**, 3761
- Owen, J. E., & Jackson, A. P. 2012, *MNRAS*, **425**, 2931
- Owen, J. E., & Lai, D. 2018, *MNRAS*, **479**, 5012
- Owen, J. E., & Wu, Y. 2017, *ApJ*, **847**, 29
- Pai Asnodkar, A., Wang, J., Gaudi, B. S., et al. 2022, *AJ*, **163**, 40
- Patra, K. C., Winn, J. N., Holman, M. J., et al. 2020, *AJ*, **159**, 150
- Paxton, B., Bildsten, L., Dotter, A., et al. 2011, *ApJS*, **192**, 3
- Paxton, B., Cantiello, M., Arras, P., et al. 2013, *ApJS*, **208**, 4
- Paxton, B., Schwab, J., Bauer, E. B., et al. 2018, *ApJS*, **234**, 34
- Paxton, B., Smolec, R., Schwab, J., et al. 2019, *ApJS*, **243**, 10
- Pereira, F., Grunblatt, S. K., Psaridi, A., et al. 2024, *MNRAS*, **527**, 6332
- Persson, C. M., Georgieva, I. Y., Gandolfi, D., et al. 2022, *A&A*, **666**, A184
- Petigura, E. A. 2015, PhD thesis, University of California, Berkeley
- Price-Whelan, A. M., Sipőcz, B. M., Günther, H. M., et al. 2018, *AJ*, **156**, 123
- Riello, M., De Angeli, F., Evans, D. W., et al. 2018, *A&A*, **616**, A3
- Rodriguez, J. E., Quinn, S. N., Zhou, G., et al. 2021, *AJ*, **161**, 194
- Rosenthal, L. J., Fulton, B. J., Hirsch, L. A., et al. 2021, *ApJS*, **255**, 8
- Rowell, N., Davidson, M., Lindegren, L., et al. 2021, *A&A*, **649**, A11
- Rustamkulov, Z., Sing, D. K., Mukherjee, S., et al. 2023, *Natur*, **614**, 659
- Salvatier, J., Wiecki, T. V., & Fonnesbeck, C. 2016, *PeerJ Comp. Sci.*, **2**, e55
- Salz, M., Czesla, S., Schneider, P. C., & Schmitt, J. H. M. M. 2016, *A&A*, **586**, A75
- Saunders, N., Grunblatt, S. K., Huber, D., et al. 2022, *AJ*, **163**, 53
- Schwab, C., Rakich, A., Gong, Q., et al. 2016, *Proc. SPIE*, **9908**, 99087H
- Serrano, L. M., Gandolfi, D., Mustill, A. J., et al. 2022, *NatAs*, **6**, 736
- Shematovich, V. I., Ionov, D. E., & Lammer, H. 2014, *A&A*, **571**, A94
- Skrutskie, M. F., Cutri, R. M., Stiening, R., et al. 2006, *AJ*, **131**, 1163
- Soares-Furtado, M., Cantiello, M., MacLeod, M., & Ness, M. K. 2021, *AJ*, **162**, 273
- Stassun, K. G., Oelkers, R. J., Paegert, M., et al. 2019, *AJ*, **158**, 138
- Steffansson, G., Mahadevan, S., Hebb, L., et al. 2017, *ApJ*, **848**, 9
- Sun, M., Arras, P., Weinberg, N. N., Troup, N. W., & Majewski, S. R. 2018, *MNRAS*, **481**, 4077
- Tayar, J., Clayton, Z. R., Huber, D., & van Saders, J. 2022, *ApJ*, **927**, 31
- Tayar, J., Stassun, K. G., & Corsaro, E. 2019, *ApJ*, **883**, 195
- Theano Development Team 2016, arXiv:[1605.02688](https://arxiv.org/abs/1605.02688)
- Thorngren, D. P., Fortney, J. J., Lopez, E. D., Berger, T. A., & Huber, D. 2021, *ApJL*, **909**, L16
- Thorngren, D. P., Fortney, J. J., Murray-Clay, R. A., & Lopez, E. D. 2016, *ApJ*, **831**, 64
- Thorngren, D. P., Lee, E. J., & Lopez, E. D. 2023, *ApJL*, **945**, L36
- Torra, F., Castañeda, J., Fabricius, C., et al. 2021, *A&A*, **649**, A10
- Turner, J. D., Ridden-Harper, A., & Jayawardhana, R. 2021, *AJ*, **161**, 72
- Van Eylen, V., Albrecht, S., Huang, X., et al. 2019, *AJ*, **157**, 61
- Vidal-Madjar, A., Désert, J. M., Lecavelier des Etangs, A., et al. 2004, *ApJL*, **604**, L69
- Villaver, E., Livio, M., Mustill, A. J., & Siess, L. 2014, *ApJ*, **794**, 3
- Vissapragada, S., Chontos, A., Greklek-McKeon, M., et al. 2022a, *ApJL*, **941**, L31
- Vissapragada, S., Knutson, H. A., Greklek-McKeon, M., et al. 2022b, *AJ*, **164**, 234
- Vogt, S. S., Allen, S. L., Bigelow, B. C., et al. 1994, *Proc. SPIE*, **2198**, 362
- Wang, L., & Dai, F. 2021, *ApJ*, **914**, 99
- Watson, A. J., Donahue, T. M., & Walker, J. C. G. 1981, *Icar*, **48**, 150
- Weinberg, N. N., Davachi, N., Essick, R., et al. 2024, *ApJ*, **960**, 50
- Weinberg, N. N., Sun, M., Arras, P., & Essick, R. 2017, *ApJL*, **849**, L11
- Weiss, L. M., Dai, F., Huber, D., et al. 2021, *AJ*, **161**, 56
- Wright, E. L., Eisenhardt, P. R. M., Mainzer, A. K., et al. 2010, *AJ*, **140**, 1868
- Yee, S. W., Winn, J. N., Hartman, J. D., et al. 2022, *AJ*, **164**, 70
- Yee, S. W., Winn, J. N., Knutson, H. A., et al. 2020, *ApJL*, **888**, L5
- Yoshida, S., Vissapragada, S., Latham, D. W., et al. 2023, *AJ*, **166**, 181
- Zahn, J. P. 1977, *A&A*, **57**, 383